2020

Strengthening mechanisms in nickel-copper alloys: A review

Olexandra Marenych
University Of Wollongong, om753@uowmail.edu.au

Andrii Kostryzhev
University of Wollongong, andrii@uow.edu.au

Strengthening mechanisms in nickel-copper alloys: A review

Abstract

© 2020 by the authors. Licensee MDPI, Basel, Switzerland. Nickel-Copper (Ni-Cu) alloys exhibit simultaneously high strength and toughness, excellent corrosion resistance, and may show good wear resistance. Therefore, they are widely used in the chemical, oil, and marine industries for manufacturing of various components of equipment, such as: Drill collars, pumps, valves, impellers, fixtures, pipes, and, particularly, propeller shafts of marine vessels. Processing technology includes bar forging, plate and tube rolling, wire drawing followed by heat treatment (for certain alloy compositions). Growing demand for properties improvement at a reduced cost initiate developments of new alloy chemistries and processing technologies, which require a revision of the microstructure-properties relationship. This work is dedicate to analysis of publicly available data for the microstructure, mechanical properties and strengthening mechanisms in Ni-Cu alloys. The effects of composition (Ti, Al, Mn, Cr, Mo, Co contents) and heat treatment on grain refinement, solid solution, precipitation strengthening, and work hardening are discussed.

Disciplines

Engineering | Science and Technology Studies

Publication Details

Marenych, O. & Kostryzhev, A. (2020). Strengthening mechanisms in nickel-copper alloys: A review. Metals, 10 (10), 1-18.

metals

MDPI

Review

Strengthening Mechanisms in Nickel-Copper Alloys: A Review

Olexandra Marenych and Andrii Kostryzhev *

School of Mechanical, Materials, Mechatronic and Biomedical Engineering, University of Wollongong, Wollongong, NSW 2500, Australia; om753@uowmail.edu.au

* Correspondence: andrii@uow.edu.au; Tel.: +61-02-4221-3034

Received: 2 September 2020; Accepted: 30 September 2020; Published: 12 October 2020

Abstract: Nickel-Copper (Ni-Cu) alloys exhibit simultaneously high strength and toughness, excellent corrosion resistance, and may show good wear resistance. Therefore, they are widely used in the chemical, oil, and marine industries for manufacturing of various components of equipment, such as: drill collars, pumps, valves, impellers, fixtures, pipes, and, particularly, propeller shafts of marine vessels. Processing technology includes bar forging, plate and tube rolling, wire drawing followed by heat treatment (for certain alloy compositions). Growing demand for properties improvement at a reduced cost initiate developments of new alloy chemistries and processing technologies, which require a revision of the microstructure-properties relationship. This work is dedicate to analysis of publicly available data for the microstructure, mechanical properties and strengthening mechanisms in Ni-Cu alloys. The effects of composition (Ti, Al, Mn, Cr, Mo, Co contents) and heat treatment on grain refinement, solid solution, precipitation strengthening, and work hardening are discussed.

Keywords: Ni-Cu alloys; microstructure characterisation; mechanical properties; strengthening mechanisms

1. Introduction

The Ni-Cu system forms the basis for the Monel alloy family (Table 1). Monel was discovered by Robert Crooks Stanley who was employed by the International Nickel Company (INCO) in 1901. The new alloy was named in honour of the company president, Ambrose Monell. The name is now a trademark of Special Metals Corporation [1].

Table 1. Chemical compositions of Monel alloys (wt.%).

Monel Alloys		Ni	Cu	C	Mn	Fe	Co	S	Si	Al	Ti
Monel 400	Max	-	34.0	0.3	2.0	2.5	-	0.024	0.5	-	-
	Min	63.0	28.0	-	-	-	-	-	-	-	-
Monel 401	Max	45.0	Balance	0.1	2.25	0.75	0.25	0.015	0.25	-	-
	Min	40.0	-	-	-	-	-	-	-	-	-
Monel 404	Max	57.0	Balance	0.15	0.1	0.5	-	0.024	0.1	0.05	-
	Min	52.0	-	-	-	-	-	-	-	-	-
Monel R405	Max	-	34.0	0.3	2.0	2.5	-	0.060	0.5	-	-
	Min	63.0	28.0	-	-	-	-	0.025	-	-	-
Monel K500	Max	-	33.0	0.18	1.5	2.0	0.25	0.006	0.5	3.15	0.85
	Min	63.0	27.0	-	-	-	-	-	-	2.3	0.35

Ni and Cu exhibit very similar atomic characteristics. They both have face centred cubic (fcc) crystal structure type, less than three percent difference in atomic radii, and exhibit similar electronegativity

and valence state. The Ni-Cu system has complete solid solubility, which allows production of single phase alloys over the entire composition range [2]. Although the Ni-Cu system exhibits complete solid solubility [3], the large differences in melting points between Ni (1455 °C) and Cu (1085 °C) can result in Cu segregation. Following equilibrium solidification at slow cooling rates, dendrites become enriched in Ni and interdendritic regions get enriched in Cu [4–6]. However, with an increase in cooling rate during solidification the compositional gradient decreases and the microstructure morphology changes from dendritic to cellular [7]. Higher undercoolings during solidification also lead to finer and more equiaxed grain sizes after annealing [8].

Monel alloys can be easily fabricated by hot and cold metal forming processes and machining. Recrystallisation studies determined the optimum hot deformation temperatures to be 950–1150 °C [9,10], which are quite similar to other Ni-base alloys and steels. However, heat treatment schedule requires rigorous development: usually a two-step age-hardening heat treatment in the temperature range of 650–480 °C is used for Ni-Cu alloys [11,12]. The higher temperature stage helps to quickly nucleate precipitates of alloying elements, and the lower temperature stage provides a superior distribution of higher number density of smaller-sized particles. Ni-Cu alloys are usually quite weldable to each other and to other Ni alloys and stainless steels [13,14]. Lower heat inputs produce finer grain microstructures with random texture and higher strength and ductility [15]. Monel alloys are expensive, with their cost reaching up to 3 times that of Ni and 7 times that of Cu [16–18]. Hence their use is limited to those applications where they cannot be replaced with a cheaper alternative.

Major additions of copper (28–40 wt.%) improve corrosion resistance of Ni in many agents, in particular nonoxidizing acids, nonaerated sulphuric and hydrofluoric acids [19–21]. This determines areas of application of Ni-Cu alloys. They are widely used for manufacturing various components of equipment in chemical, oil and marine industries (such as drill collars, pumps, valves, fixtures, piping, fasteners, screws, propeller shafts, steam generators, turbines [22–27]), for protective coating [28,29], for manufacturing electrical and electronic equipment (resistors, bimetal contacts, capsules for transistors and ceramic-to-metal sealing [30,31]), and in fuel cells [32,33].

2. Role of Alloying Elements

Ni can dissolve high concentrations of alloying elements compared to other metals [34]. Alloying elements increase mechanical strength via solid solution [35–40] or precipitation strengthening [41–45]. However, the solid solution strengthening effect of Cu is much lower compared to other elements [19,46]. For example, in recently developed nanocrystalline Ni-Cu alloys both strength and ductility increased with Cu content by only 40% for Cu concentrations increasing by 5 times (from 6 to 32 wt.%) [47]. This was associated with grain refinement and solid solution strengthening. Work hardening also increased with Cu content, as the stacking fault energy decreased, leading to increased dislocation densities and twinning. Due to the substantial increase in strength-to-weight ratio, achieved by precipitation hardening, the weight of turbine engines was significantly reduced, which enhanced development of the aerospace industry [22]. Although Ti and Al provide some solid solution strengthening effect, they typically improve strength by precipitation of γ'-Ni_3(Ti,Al) particles during heat treatment [19,48]. Aluminium (2.3–3.15%) provides excellent corrosion resistance resulting from the formation of a protective Al_2O_3 surface oxide layer. Titanium (0.35–0.85%) forms TiC carbides [49]. Together Al and Ti are often used in minor amounts to increase corrosion resistance via deoxidation [20]. They both combine with oxygen to form oxides, thus controlling porosity in welds [2]. Carbon (<0.25 wt.%) is required for carbide formation, which not only increase strength at room temperature but also creep resistance [50]. Manganese (<1.5%) improves corrosion resistance and weldability, promotes formation of $M_{23}C_6$ type carbides [3,51]. Iron (<2.0%) provides solid solution strengthening at reduced costs, but may be detrimental for corrosion resistance [20]. Fe also increases the solubility of C in Ni; this improves resistance to high-temperature carburizing environments [19]. Cobalt (<0.25%) increases high-temperature strength via solid solution strengthening, and resistance to carburization and sulphidation [20]. Additions of Co also raise solvus temperature of γ' phase [19]. Sulphur

(<0.006%) enhances machinability [52]. Silicon (<0.5%) is typically present only in minor amounts as a residual element from deoxidation or as an intentional addition to promote high-temperature oxidation resistance [19].

3. Microstructure

Ni-Cu alloys have fcc matrix (γ) with a lattice parameter of 0.3534 nm [53]. Due to full mutual solubility of Ni and Cu, the second phase does not form (Figure 1), although particles of various chemistries can precipitate. Therefore, in this alloy strengthening occurs via four mechanisms: grain refinement, solid solution, precipitation and dislocation strengthening (work hardening). Grain refinement is achieved as a result of recrystallization during hot deformation in the 870–1150 °C temperature range [54]. A required level of precipitation strengthening is usually obtained after age hardening heat treatment. Dislocation strengthening follows cold rolling or drawing [55–57].

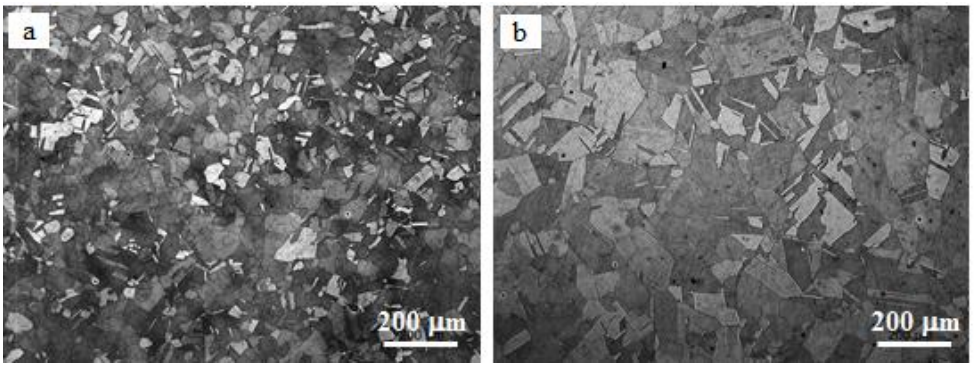

Figure 1. Typical microstructure of Monel K500 rod in (**a**) hot rolled and (**b**) annealed at 1100 °C for 15 min conditions (the authors' unpublished data).

After an appropriate heat treatment, the following intermetallic particles can precipitate: $Ni_3(AlX)$, Ni_3Ti, and $NiFe_3(AlFe)$ [49,58]. $Ni_3(Al,X)$ particles, where X can be Cu, Mn, Ti, or Si, are known as gamma prime precipitates (γ'). Gamma prime (γ') particles have an ordered fcc crystal structure (Figure 2a) with close crystallographic matching to the Ni fcc matrix (<1% mismatch) [59]. The Al atoms occupy the cube corners while the Ni ones reside on the face centres. In Ni-Cr-Fe alloys Co and Fe can substitute Ni [60], while Cu, Mn, and Si tend to substitute Al. Gamma prime particles homogeneously nucleate through the volume, and maintain spherical shape and coherency with the Ni matrix even after many hours of aging (Figure 3). The precipitates do not show any tendency for alignment or nucleation at dislocations. Close crystallographic matching between the γ matrix and γ' precipitates leads to a very low surface energy that, consequently, results in very low particle coarsening rates and increased number density of fine particles [61]. The coarsening process is controlled by bulk diffusion of the γ'-forming elements. The activation energy of the coarsening process is close to that of diffusion of Al in Ni. The average γ' particle radius remains proportional to the cube root of ageing time. The volume fraction of precipitates can reach 6–7% after aging at 700 °C [49].

The Ni-Al and Ni-Ti phase diagrams (Figure 4) can help to analyse precipitation in Ni-base alloys [62]. Most Ni-base alloys contain below 10 wt.% of (Al + Ti). However, even minor additions of Al or Ti result in precipitation of Ni_3Al or Ni_3Ti particles. The γ' solvus temperature is ranging between 700 and 750 °C for the solution treated and quenched alloys [49]. Therefore, the solution annealing temperature is usually above 950 °C. The solubility temperature of γ' particles in Monel is relatively lower compared with those in high temperature precipitation strengthened Ni-base superalloys. This is associated with much lower Al and Ti contents in Monel K500 compared to Al, Ti, Nb, and Ta concentrations in other Ni-base alloys [63]. Decomposition of the supersaturated austenite may not occur during quenching, meaning that even very fine nano-scale particles do not precipitate [49]. This is contrarily to other Ni-Al and Ni-Ti alloys, where γ' forms readily on

quenching [64,65]. The substitution of some neighbouring elements in the periodic table (Cr, Fe, and Co) for Ni in alloy composition is known to decrease γ′ solubility and increase the γ′-particle volume fraction even for the same Al + Ti contents [66]. Precipitation of γ′ in Monel K500 at 750 °C, while the solubility of Al in Ni at this temperature is quite high and is reaching 5 wt.% in binary Ni-A1 system, suggests that Cu also decreases the solubility of γ′ [67]. The γ′ precipitation provides significant strengthening effect with temperatures increasing up to ~800 °C [68]. This is believed to occur due to ordering in the particle lattice and the relatively low mobility of super lattice dislocations that occurs with increasing temperature.

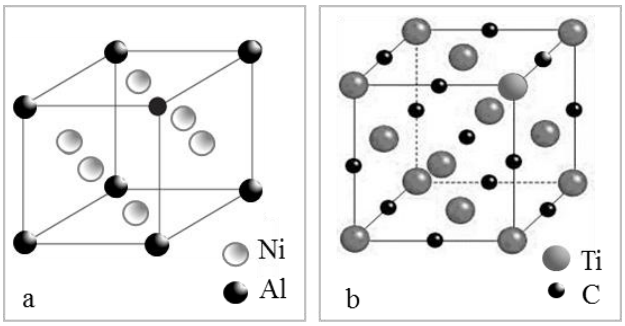

Figure 2. (**a**) Ordered face centred cubic (fcc) crystal structure of a γ′-Ni_3(Ti,Al) particle and (**b**) TiC particle.

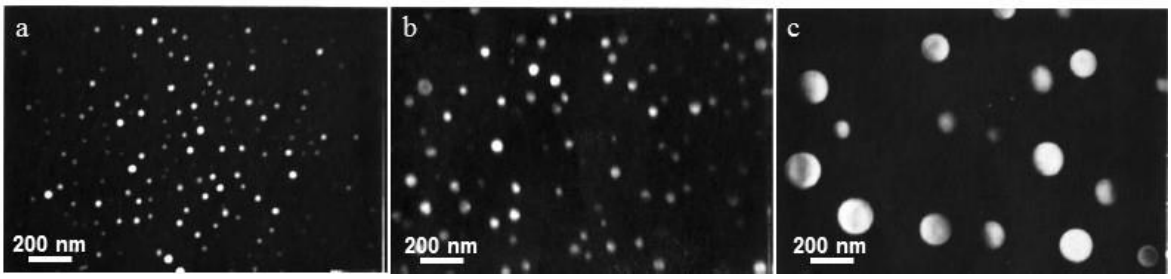

Figure 3. TEM dark field images illustrating the homogeneous distribution and the spherical shape of the γ′ precipitates retained even after prolonged aging at 700 °C for (**a**) 64 h, (**b**) 128 h, and (**c**) 1000 h [49].

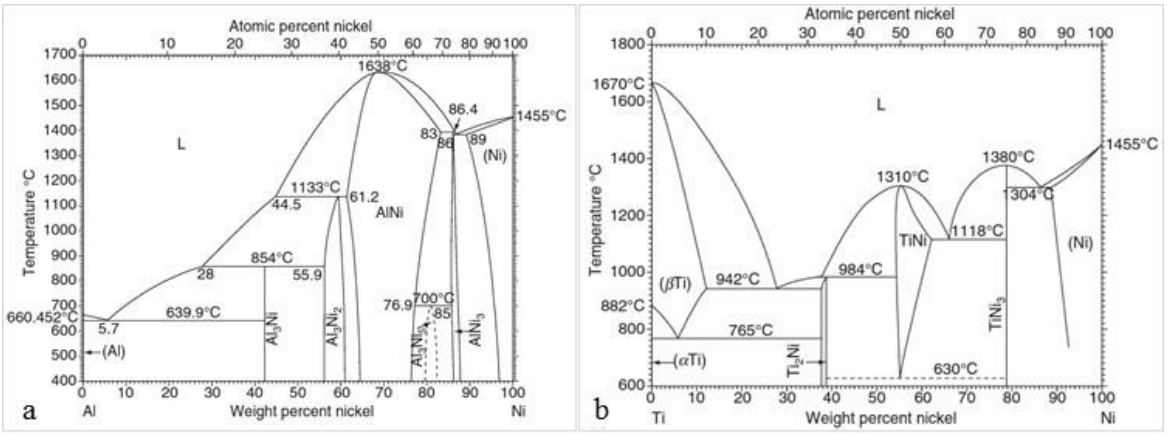

Figure 4. Binary (**a**) Ni-Al and (**b**) Ni-Ti phase diagrams [62].

The Ni_3Ti phase, designated as eta (η), exhibits stoichiometric composition of 75 at.% Ni-25 at.% Ti and a stable hexagonal closed packed crystal structure. Although the η-Ni_3Ti particles may have ordered metastable fcc structure at lower temperatures. Ti additions promote formation of the η-Ni_3Ti phase, while Al additions promote formation of the γ′-Ni_3Al phase. The hexagonal η-Ni_3Ti usually

appears as coarse disk-shaped particles of low number density that does not provide reasonable strengthening. Thus, fine γ′-Ni_3Al particles of high number density are preferred [68].

Appreciable C levels, 0.18 wt.% in Monel K500, result in precipitation of carbides. Carbides composition, size, and number density depend on the alloy composition and processing history, and may vary in service [2]. The Ti-rich MC carbide is the main carbide phase in Monel K500, (Figure 2b). Coarse TiC particles randomly precipitate within the grains or along the grain boundaries (Figure 5) [69]. They possess the fcc crystal structure and usually form at the end of solidification by the eutectic-type reaction [70]. The morphology and distribution of TiC do not change with heat treatment below 980 °C. However, these particles may slightly grow during heat treatment [69]. TiC do not easily dissolve during re-heating for metal forming operations and, thus, may appear as stringers along the rolling direction. The MC carbides can often be replaced by $M_{23}C_6$ carbides during thermomechanical processing or high temperature service [48]. Due to absence of Cr, the $M_{23}C_6$ carbides in Monel K500 are generally Mn rich and precipitate in the temperature range of 760–980 °C. These carbides preferentially form on grain boundaries and, thus, can improve creep resistance via restricting grain boundary migration (Figure 5c). Presence of carbides retards recrystallization, refines grain size, and improves the high temperature strength and ductility. However, the carbides type and morphology should be carefully controlled to avoid fracture initiation at the particle-matrix interface during a component manufacturing or in service [71]. The MCN carbonitrides are similar to MC carbides in morphology and crystallography, except that substantial levels of C are substituted by N. The eutectic-type reactions leading to formation of carbides and carbonitrides are facilitated by the strong tendency of C, N, and Ti to segregate to the liquid during solidification. As a result, carbonitrides may precipitate in the interdendritic regions and grain boundaries [71,72]. Recent studies of boron addition to Monel 400 showed a possibility to increase hardness by 4 times (from 200 HV to 800 HV) and wear resistance by 60% following precipitation of Ni borides [73,74].

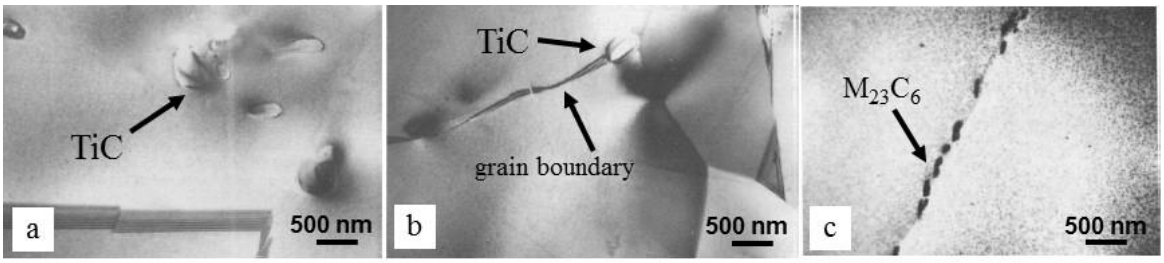

Figure 5. Particle precipitation: (**a**) TiC within the grains, (**b**) TiC at the grain boundaries, and (**c**) $M_{23}C_6$-type carbides at the grain boundaries [69].

A moderate density of dislocations have been observed in Monel K500 thin (0.2 mm) sheets that were solution annealed, aged, and water quenched [49]. It was proposed that the dislocations were formed following micro-deformations under the quenching stresses. These dislocations of moderate density did not exhibit any distribution pattern in the form of planar arrays or pairing. This suggests a quite high level of stacking fault energy of the alloy and absence of short-range ordering in the solution-annealed and quenched material. The arrangement of dislocations in the solution-treated and deformed (3% strain) specimens was found to be nonplanar in several regions of the grains (Figure 6a) [49]. Although the stacking fault energy of Ni alloys is high [75], alloying may decrease this value, as has been observed, for example, in many Ni-Cr-base alloys [76]. However, Cu additions to Ni do not reduce the stacking fault energy of the alloy [77,78]. The concentrations of other alloying elements in Monel K500 are too low to substantially reduce the stacking fault energy of the matrix [49]. Therefore, deformation twins are usually not observed. However, annealing twins do form (Figure 6b). Annealing twins in Monel K500 are prevalent in solution annealed, water quenched, air-cooled, or aged material [49,72]. The solution annealed alloy was found to contain a moderate density of annealing twins, which usually appeared as parallel bands bounded by coherent (111) planes.

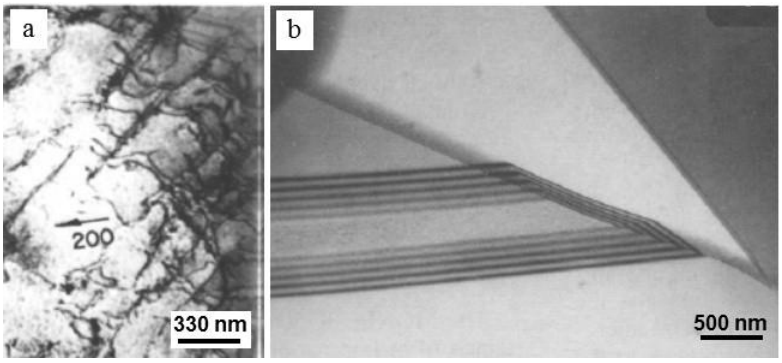

Figure 6. (**a**) Non-planar dislocation arrangement in a slightly deformed (3% strain) sample [49] and (**b**) annealing twins in the fully annealed Monel K500 [69].

4. Strengthening Mechanisms

As Monel K500 is a single phase alloy, four strengthening mechanisms operate in it: grain refinement, solid solution, precipitation, and dislocation strengthening (work hardening). Depending on the microalloying element content (in particular, Ti, Al, Co, Fe) and processing schedule (age hardening heat treatment), either the solid solution strengthening or precipitation strengthening dominates.

4.1. Grain Refinement

Figure 7a shows an example of grain size strengthening in Monel 400. With an increase in grain size from 9.5 to 202 μm the stress-strain curve moves downwards along the stress axis and the yield stress value decreases from about 290 to 130 MPa. However, this variation in grain size did not affect the work-hardening behaviour, i.e., the stress-strain curves for all the grain sizes are essentially parallel. Independence of work hardening rate on grain was observed in other fcc metals, especially at low initial dislocation densities, when a possible dislocation accumulation at grain boundaries does not restrict the dislocation motion in the grain interior [79]. With strain rate increasing from the quasi-static to dynamic, the stress-strain curves move up along the stress axis (Figure 7b); a similar trend was observed in other fcc materials [80]. However, the effect of strain rate on the stress-strain curve dependence on grain size is weak: the work hardening rate at a high strain rates remains invariant of grain size [81].

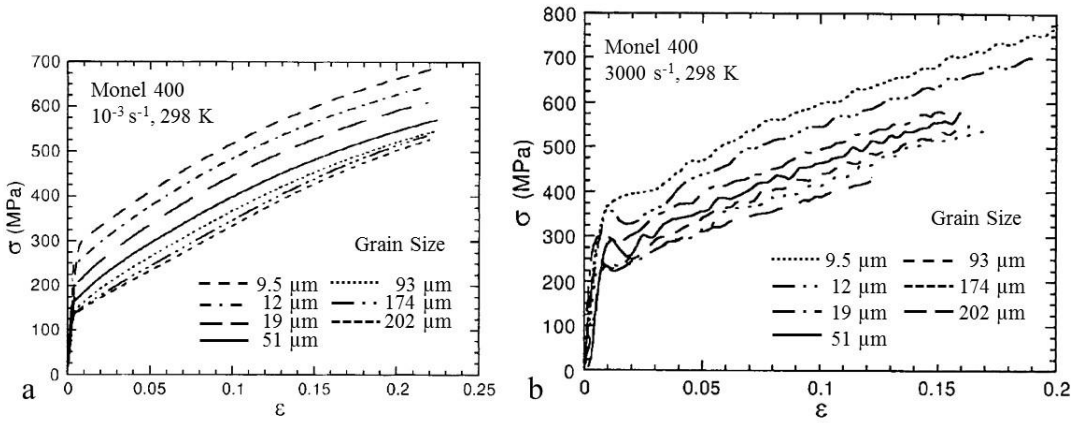

Figure 7. The stress-strain curves of Monel 400 for various grain sizes at (**a**) low and (**b**) high strain rates [81].

4.2. Solid Solution Strengthening

The solid solution strengthening effect is known to increase with the atomic size difference between the primary element and a solute. Addition of the substitutional alloying elements results in expansion of the fcc lattice leading to strengthening [46,82]. Table 2 summarizes approximate atomic diameter variations between Ni and some other elements and solubility data for these elements in Ni at 1000 °C. As can be seen, Ta, W, Mo, Ti, V, Cr, and Mn provide the best combination of atomic radii mismatch and appreciable solubility needed for solid solution strengthening. Therefore, Mo, Ti, Cr, and Mn are frequently used in many single phase Ni-base alloys for solid solution strengthening. Fe, Co and Cu also can be used for solid solution strengthening due to their high solubility in Ni [83]. The solid solution strengthening from additions of these elements will be effective only if the element concentrations do not exceed their solubility limits in Ni-based austenite, otherwise particle precipitation will take place. Although Ti, Al, and Nb can be effective solid solution strengtheners, they typically improve strength via precipitation of γ'-Ni_3(Ti,Al) or Ni_3Nb intermetallic particles, or carbides [2]. In addition to the atomic size misfit, electron configuration [84], diffusion coefficients [39], and γ-γ' lattice misfit (dependent on element partitioning between γ-matrix and γ'-particles) [85] were shown to influence the solid solution strengthening at high temperatures. Thus, slow diffusing elements Re, Os, Ir, Tc, Ru, and W provide the best high temperature strength and creep resistance.

Table 2. Approximate atomic size variations and solubility limits of some elements in Ni.

Element	Approximate Atomic Size Difference Compared to Ni, %	Approximate Solubility in Ni at 1000 °C, wt.% [34]
Ta	−51	14
W	−44	38
Mo	−41	34
Ti	−27	10
V	−22	20
Cr	−17	40
Mn	−12	20
Nb	−49	6
Al	31	7
Si	38	8
C	82	0.2
Fe	−9	100
Co	−3	100
Cu	4	100

4.3. Precipitation Strengthening

In Monel K500 significant hardening is associated with the precipitation of gamma prime (γ') particles. The γ' precipitates have an ordered fcc crystal structure; therefore, the dislocation interaction mechanisms with the ordered precipitates dictate the level of strengthening. Initially, the particles nucleate and grow at a relatively short distance from each other. In this case of small interparticle spacing the particle shearing mechanism prevails. With coarsening, as the interparticle spacing increases, dislocation looping between the particles starts dominating. When precipitate shearing occurs, the strengthening of an alloy can arise from the (a) lattice mismatch between particles and the matrix, (b) order hardening, and (c) modulus mismatch. In Monel K500, the order hardening prevails over other shearing mechanisms. The lattice mismatch contribution to the total precipitation strengthening effect is small, because the coherency strain value is extremely small (less than 0.003) [69]. The precipitation strengthening mechanism may change with aging, due to the precipitate size variation with aging. In the under-aged and peak-aged condition, precipitation strengthening is governed predominantly by the particle shearing. This is associated with a lower shear stress required for particle shearing compared to the Orowan stress arising during looping of dislocations around precipitates [86].

In the overaged condition, two processes may operate simultaneously or one after another: (i) shearing in slightly overaged conditions and (ii) looping in significantly overaged conditions. When a dislocation pair approaches a particle surrounded by a loop, the first dislocation is blocked by this dislocation loop. The second dislocation approaching the first increases the shear stress between the first dislocation and the loop. Consequently, the particle shearing (accompanied by the loop annihilation) occurs even when the looping mechanism dominates. Thus, planar slip may be observed in an alloy containing slightly overaged γ' particles. The reduction in stress due to the coarsening of precipitates is compensated by the transition of dislocation pairs to single dislocations, and thus, there is a net increase in strength in the initial stages of overaging. Order hardening originates from the interaction of dislocations with ordered precipitates (Figure 8). The cutting of an ordered precipitate by the first dislocation shifts one half of a particle crystal plane by one interatomic distance against the other half plane (Figure 8b). This results in creation of an antiphase boundary (APB) across the slip plane that represents an atomic layer of incorrect order. After the second dislocation passing through the same particle, the second shift of a crystal half plane occurs (Figure 8c,d). This restores the atomic order. Thus, dislocations travelling in pairs (often referred to as superlattice dislocations) maintain the ordered structure after precipitate shearing.

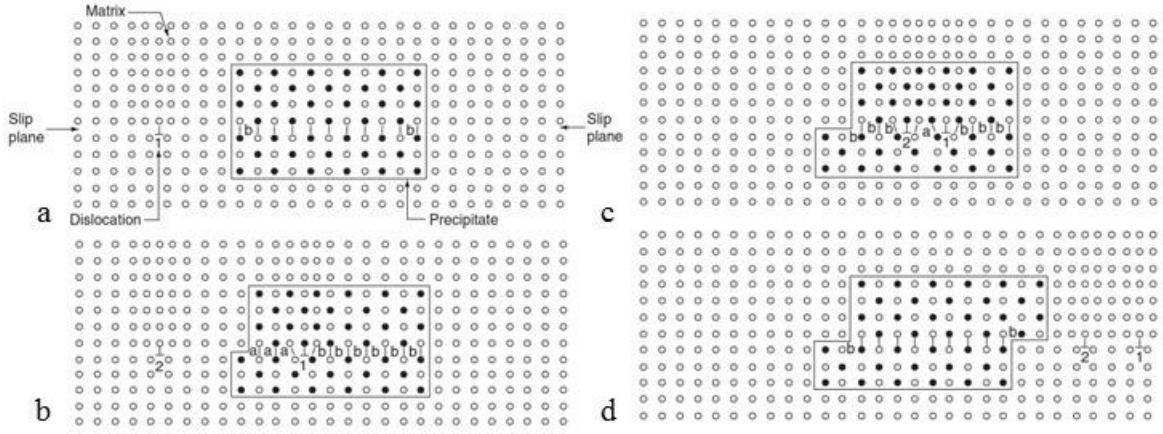

Figure 8. Schematic illustration of dislocations interacting with an ordered Ni_3Al precipitate [83]: (**a**) the original condition prior to particle cutting, (**b**) the first dislocation penetrated a particle, (**c**) the second dislocation penetrated a particle, and (**d**) shifting of one half of the particle against the other half by two interatomic distances restored the atomic order .

Figure 9 shows examples of such paired superlattice dislocations and particle cutting in a Ni-base alloy. This deformation involves cross-slip of segments of the superlattice dislocations from the {111} slip plane to {001} cross-slip plane. These cross-slipped segments cannot move without forming an APB and thus resist deformation. Strengthening from cross-slip becomes more important with increasing temperature because the cross-slip is thermally activated.

The initial cutting of an ordered particle by a single dislocation requires a stress increase. This stress increase provides energy for formation of the antiphase boundary. With increasing the antiphase boundary energy larger forces are required to cut the precipitates. Thus, the yield stress increases. The antiphase boundary energy provides a significant contribution to strengthening and was observed varying with alloy composition and particle chemistry. In particular, Ti, Co, Mo, and Fe were reported to effectively increase the antiphase boundary energy [87].

Finer particles (<20 nm) may be too small to hold two dislocations (Figure 10a), this is called a weak pair coupling. With larger particles, the second dislocation may start interacting with the particle before the first dislocation moves away (Figure 10b), this is called a strong pair coupling. In both cases, the strengthening contribution is due to the creation of an APB within the precipitate. The dislocation–particle interaction mechanism changes from shearing to looping with a particle size increase. Figure 10c qualitatively illustrates a dependence of precipitation strengthening on particle

size: this dependence shows a maximum. As the particle size varies with ageing, the precipitation strengthening contribution depends on the aging temperature and time [68]. At first, precipitation of the γ′ from the supersaturated Ni matrix leads to an increase in strength with increasing temperature and time. However, with further increase in temperature/time, an over-aging may lead to the particle coarsening and a decrease in particle volume fraction (Figure 10d). A decrease in particle volume fraction should be avoided as it results in a decrease in potential number of dislocation–particle interaction sites and strengthening capacity. Therefore, a careful design of heat treatment schedule is required to simultaneously maximise the particle size and particle volume fraction.

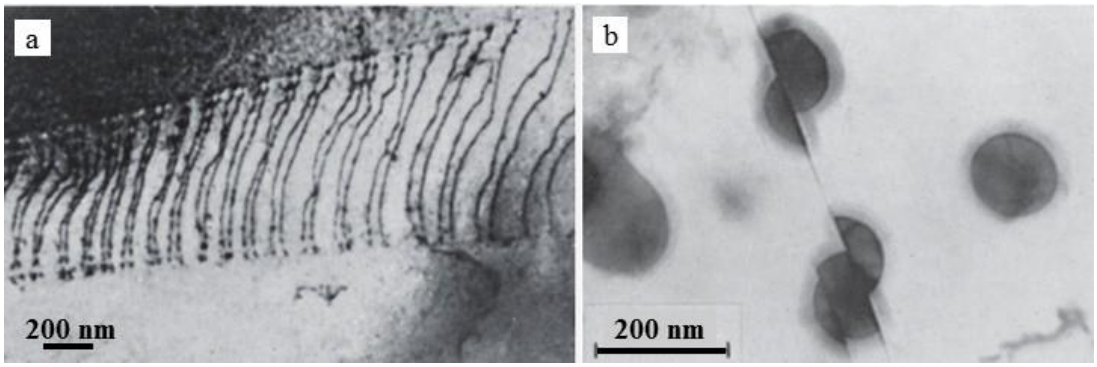

Figure 9. TEM images showing (**a**) paired super lattice dislocations and (**b**) γ′ precipitate being cut by the moving dislocations in a Ni superalloy [83].

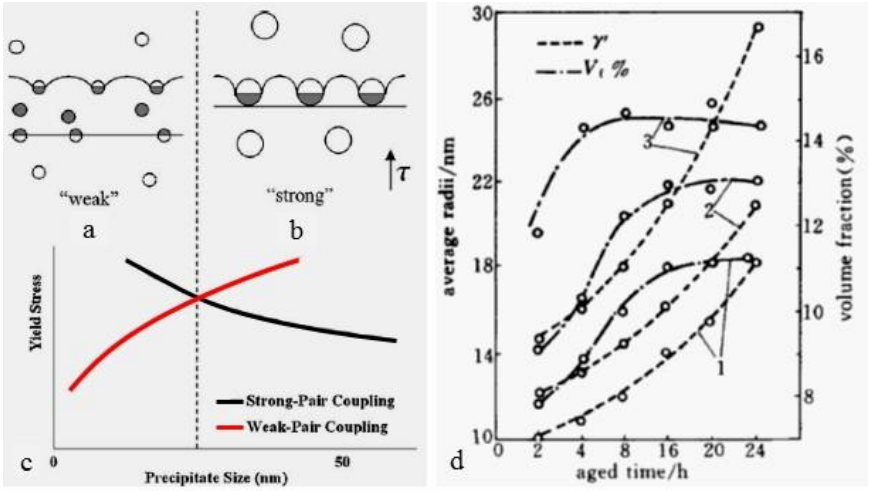

Figure 10. Schematic illustration of (**a**) weak dislocation coupling, (**b**) strong dislocation coupling, and (**c**) strengthening effect variation with particle size [46]; (**d**) effect of aging time on the γ′ size and volume fraction in Monel K500 for various aging temperatures: 1–600 °C, 2–650 °C, 3–700 °C [88].

Precipitate morphology may change with a γ/γ′ lattice mismatch (Figure 11) [89]. The precipitate shape varies to minimise strain in the vicinity of particles and the particle surface energy. At low levels of lattice mismatch, the strain is low and the spherical shape is favourable for the decrease of surface energy. At higher levels of lattice mismatch, the strain increases and becomes orientation dependent. The orientation relationship between the γ-matrix and γ′-particle promotes a cuboidal shape. These γ′-particles typically align along the <100> directions of the matrix which have the lowest elastic stiffness. The precipitate morphology also varies with coarsening. Thus, on initial stages of nucleation and growth the particles are spherical, and then gradually change to cubes, arrays of cubes, and dendritic shape as coarsening proceeds. The lattice mismatch between particles and the matrix contributes to strengthening of an alloy.

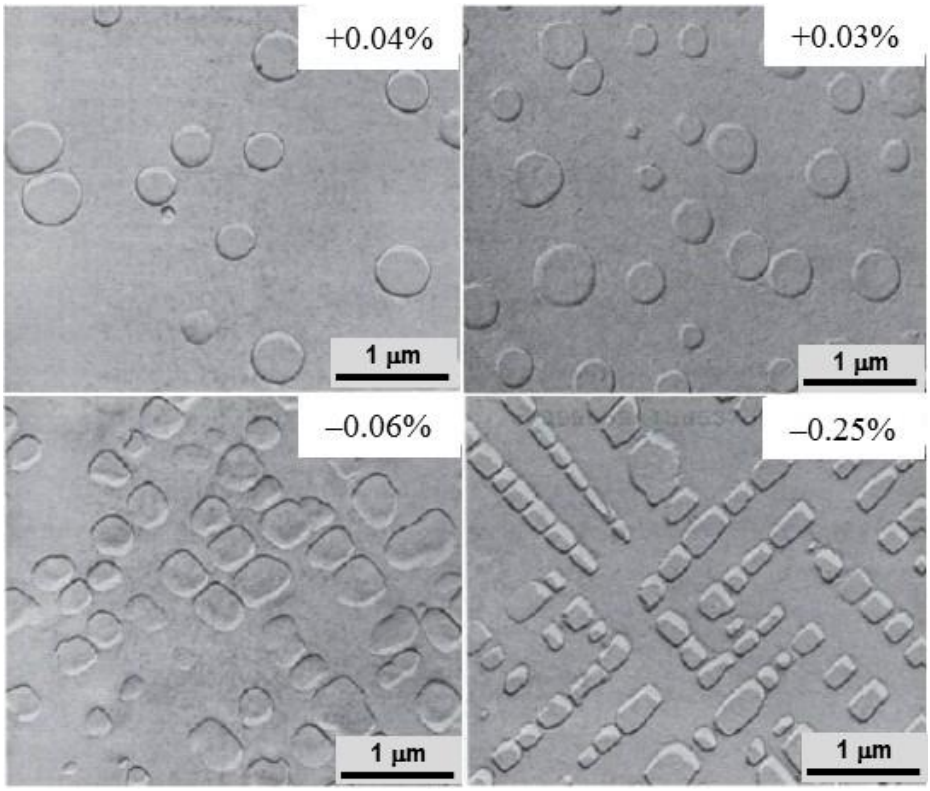

Figure 11. Optical images of γ′ particles in a Ni-Al-Mo alloy at different lattice mismatches overlaid in the top right corner [89].

The γ′ precipitates can be hardened by solid solution strengthening (Figure 12). Mo, Si, and Ti were shown to be the most effective elements for this. Although Cu and Co exhibit substantial solubility in the particles, they do not increase the strength of γ′. The lattice parameter of both the γ matrix and γ′ precipitates depends on type and concentrations of alloying elements. Various elements partition differently to the matrix and particles and change their lattice parameters. Therefore, the degree of γ/γ′ lattice mismatch depends on the relative partitioning of alloying elements and lattice parameters variations with alloying (Figure 13).

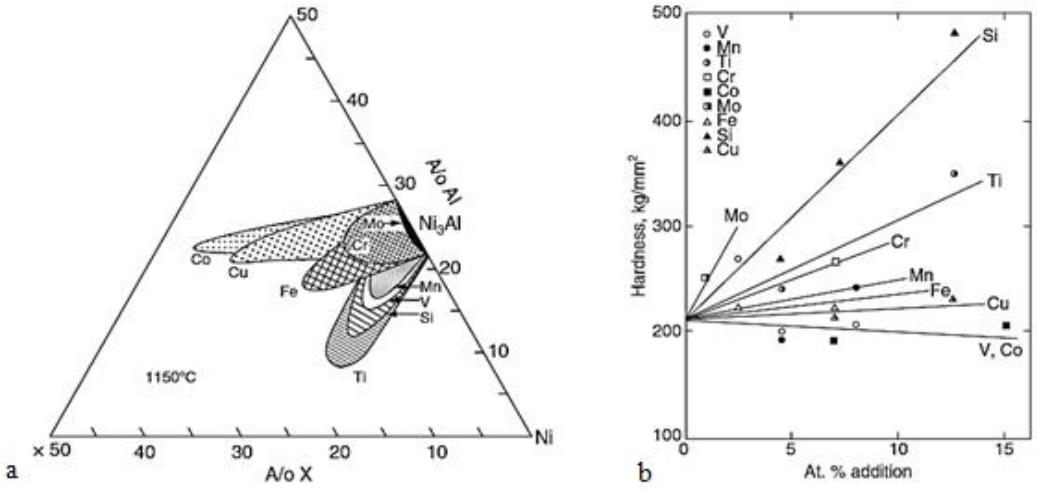

Figure 12. (**a**) Solubility of various elements in γ′ particles at 1150 °C in Ni-Al-X alloy system, (**b**) effect of various elements on the hardness of γ′ particles at 25 °C [90].

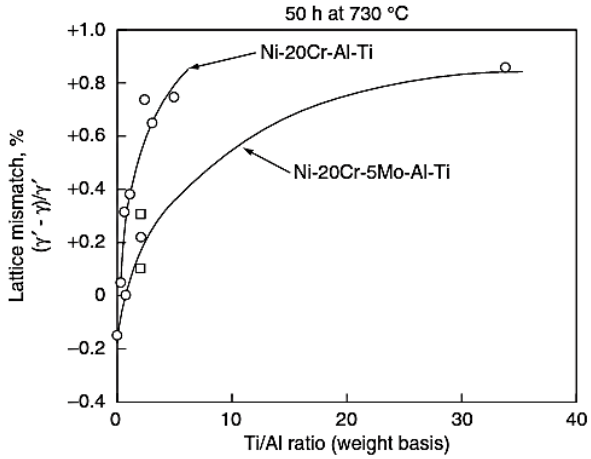

Figure 13. Effect of Ti/Al ratio on the γ/γ′ mismatch for Ni-20Cr-Al-Ti and Ni-20Cr-5Mo-Al-Ti alloys with a constant (Al + Ti) content of 3.5 wt.% [34].

4.4. Dislocation Strengthening (Work Hardening)

Ni-Cu alloys exhibit rapid work hardening, characteristic for all Ni-base alloys due to their fcc crystal structure [91]. This allows to increase the room temperature hardness and strength applying large strains of cold deformation. However, to illuminate fracture development, (i) the number of deformation passes in a processing technology should be controlled, (ii) strain per pass must be reduced with each deformation stage, and (iii) intermediate annealing should be applied to restore ductility for further processing [57].

The rate of work hardening in the presence of precipitates was found to be higher than in a precipitate-free (solution-treated) matrix and increased with increasing precipitate size [92]. In alloys where the particles were small and shearing mechanism operated, the increase in work hardening rate was minor. The passage of dislocations through particles reduced their diameters, making the passage of the following dislocations easier. A relative reduction in diameter for a small particle would be larger than that for a large particle. With growing particle size the work hardening rate increased, even when particle shearing occurred. Looping increases the work hardening rate. This can be explained by a gradual reduction in the interparticle spacing with the formation of dislocation loops around precipitates, making passage of the successive dislocations difficult [93].

With an increase in cold deformation the strength of Monel K500 increases and ductility decreases (Figure 14a). The optimum deformation strain for Monel K500 was found to be about 20% [88]: at this strain an increment to the yield stress is quite substantial (about 300 MPa) and the remaining ductility is still significant (about 30% of elongation to failure). Cold deformation has been shown to affect the strength variation during aging (Figure 14b). With an increase in aging temperature up to 600 °C, the strength increased for 0 and 10% cold worked samples. However, the samples cold worked to 20% and 25% showed strength peaks in the range of 560–600 °C followed by the strength decrease. Obviously with an increase in cold deformation the strain induced precipitation occurs faster; this leads to faster particle growth accompanied by a decrease in particle number density and strength decrease. Irrespective of the aging temperature the strength showed a minimum for 10% of prior cold worked material (Figure 14c). This could be explained if small amounts of deformation facilitated the dislocation breaking from their pinning points, increasing the dislocation mobility and decreasing the yield stress.

Since work hardening is related to solute element concentrations and presence of precipitates, the work hardening rate generally increases with complexity of alloy composition. Similarly, the age-hardenable alloys have higher work hardening rates than their solid solution equivalents [94]. In the annealed condition, Monel K500 can be cold-worked using traditional processing technology. It has excellent ductility, although deformation forces may be high. Work hardening of Monel K500

with cold deformation is shown in Figure 15 in comparison with other materials: Monel K500, precipitation hardenable with Ni_3(Ti,Al) and TiC, approaches Inconel 600, precipitation hardenable with Cr-rich carbides.

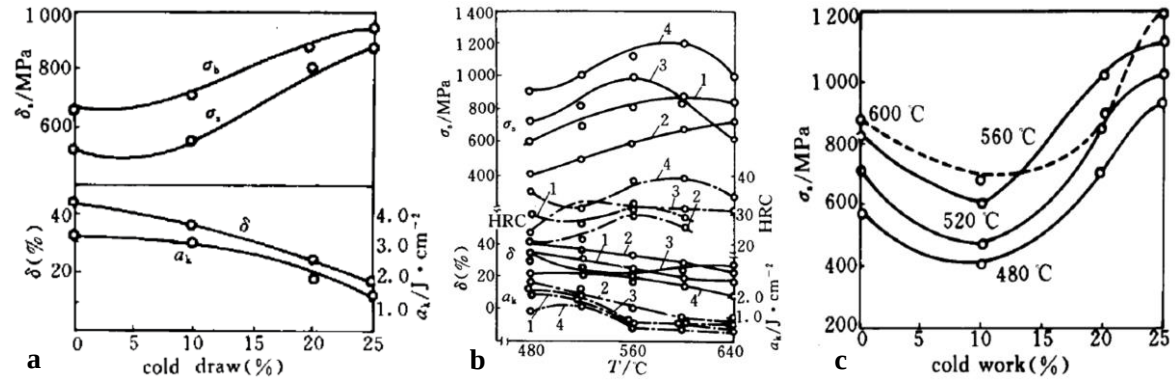

Figure 14. (**a**) Mechanical properties variation with cold deformation, (**b**) effect of age hardening temperatures on properties for various strains of prior cold deformation: 1–0, 2–0.10, 3–0.20, and 4–0.25, and (**c**) effect of prior cold deformation on the yield stress after aging at various temperatures, all for Monel K500 [88].

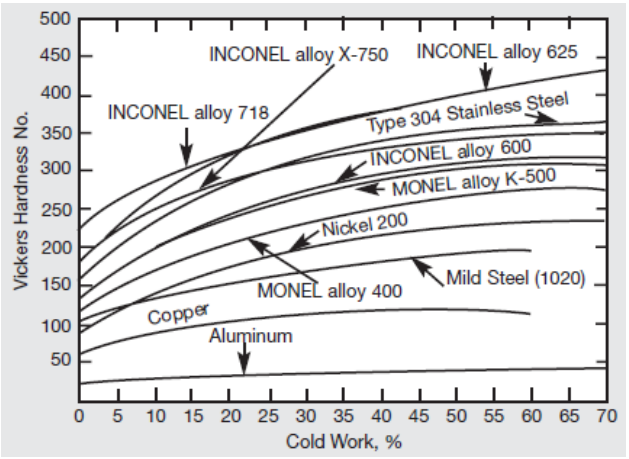

Figure 15. Comparison of work hardening capacity of Monel K500 to other Ni-base alloys [53] (reproduced with a permission from the Special Metals Corporation).

5. Mechanical Properties

Room temperature tensile properties of Monel 400 and K500 are shown in Table 3 [20]. In hot-rolled and annealed conditions Monel K500 shows a 100–200 MPa higher yield stress (YS) and ultimate tensile strength (UTS) than Monel 400, due to solid solution and precipitation strengthening. In both alloys YS and UTS are slightly higher for cold formed products, due to work hardening. In hot finished Monel K500, annealing may lead to strength decrease by about 30%, following dissolution of precipitates and dislocation annihilation. In contrast, age-hardening may result in 1.3–2.5 times increase in strength due to precipitation. For the cold formed products, annealing decreases strength by about 40–50%; although, age-hardening may increase strength by up to 1.3 times. As seen, the age-hardening heat treatment is more effective in increasing strength of the hot finished products, compared to the cold finished.

High and low temperature tensile properties of Monel K500 are shown in Figure 16. For hot rolled product, with an increase in temperature the YS and UTS do not vary significantly until 650 °C (1200 °F) and 150 °C (300 °F), respectively. Age-hardening increases YS and UTS by about 1.5 and 2 times, respectively. However, the YS stability at high temperature decreases, YS starts going down at a lower temperature of 430 °C (800 °F) compared to the non-aged material. In contrast, the stability of UTS

increases, UTS starts decreasing at a higher temperature of 300 °C (550 °F) compared to the non-aged material. The decrease in YS stability after ageing can be associated with destruction of the dislocation sub-structure during ageing, and the increase in UTS stability follows particle precipitation. Annealing prior age-hardening does not provide any strength gain compared to the hot-rolled and age-hardened product, however the stability of elongation increase. This is a consequence of significantly reduced dislocation density after annealing and increased distance of dislocations free pass. With a decrease in temperature, the tensile strength and yield stress both increase while ductility and toughness remain virtually the same (Figure 16d). No ductile-to-brittle transition occurs even at temperatures as low as that of liquid hydrogen. Thus, this alloy is suitable for many cryogenic applications.

Table 3. Mechanical properties of Monel 400 and K500 [20].

Processing Condition	Yield Strength, MPa	Tensile Strength, MPa	Elongation, %	HB
	Monel 400			
Hot-Finished	280–690	550–760	30–60	140–240
Hot-Finished, Annealed	170–340	520–620	35–60	110–150
Cold-Drawn	380–690	580–830	22–40	160–225
	Monel K500			
Hot-Finished	280–760	620–1070	45–20	140–315
Hot-Finished, Aged	690–1034	965–1310	30–20	265–346
Hot-Finished, Annealed	280–414	621–760	45–25	140–185
Hot-Finished, Annealed and Aged	586–830	896–1140	35–20	250–315
Cold-Drawn, As-Drawn	483–860	690–965	35–13	175–260
Cold-Drawn, Aged	655–1100	931–1280	30–15	255–370
Cold-Drawn, Annealed	280–414	621–760	50–25	140–185
Cold-Drawn, Annealed and Aged	586–830	896–1310	30–20	250–315

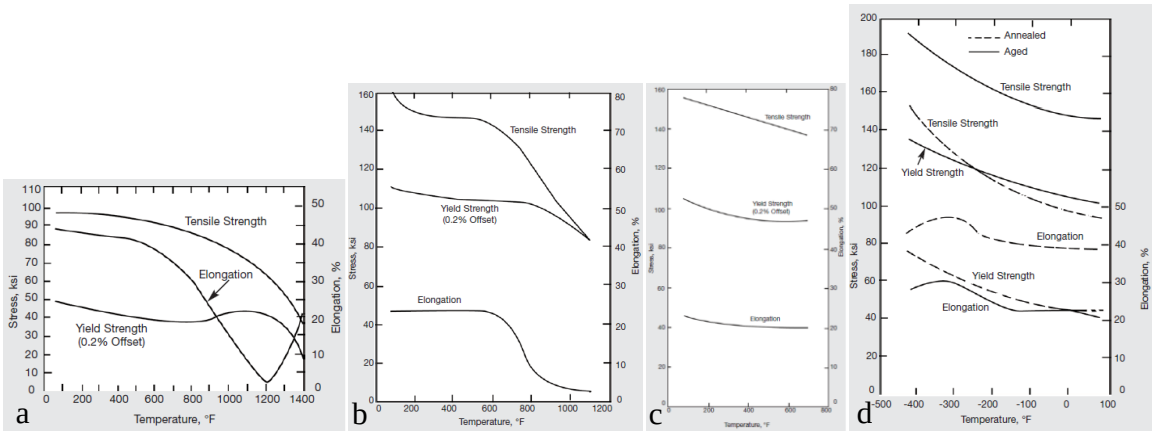

Figure 16. High temperature tensile properties of Monel K500: (**a**) hot-rolled, (**b**) hot-rolled and age-hardened, and (**c**) annealed and age-hardened; (**d**) low temperature tensile properties of Monel K500 [53] (reproduced with a permission from the Special Metals Corporation).

In view of excellent corrosion resistance coupled with high strength and toughness at cryogenic temperatures [95,96] Monel alloys are good candidates for structural components of machinery and storage of liquefied gases in aerospace and chemical industry. High temperature application of Monel is limited by low melting temperature of Cu. However, the precipitation strengthening capacity in the Ni-Cu alloy system can be improved with appropriate alloying element additions and heat treatment. Ni-Cu alloys are easily weldable [97] and were successfully used as an input material in powder based [98] and wire arc additive manufacturing [99]. Development of these modern technologies allows to apply the Ni-Cu alloys as a surface cladding material for protection of less corrosion resistant core or in components with mechanical properties gradient.

6. Conclusions

Due to Ni and Cu exhibiting complete solid solubility, their alloys are single phase. Thus, in Ni-Cu alloy four strengthening mechanisms operate: grain refinement, solid solution, precipitation, and dislocation strengthening (work hardening). Composition of an alloy determines whether the solid solution or precipitation strengthening dominates. Mo, Ti, Cr, and Mn are the most frequently used solid solution strengthening elements, due to their significant difference in atomic sizes from Ni. Such elements as Fe, Co, and Cu are the second order solid solution strengtheners, due to their high solubility in Ni. Al and Ti are the most effective precipitation strengthening elements in Ni-Cu alloys, as they tend to form NiAlTi-rich intermetallic particles. Sometimes Mn-rich $M_{23}C_6$ or Ti-rich MC carbides can also precipitate. The dislocation strengthening capacity of Ni-Cu alloys is substantial, which is determined by their fcc crystal structure. However, cold deformation above 20% would decrease ductility below the practically reasonable limits of 30% elongation. In presence of particle forming elements in alloy composition, age hardening heat treatment is frequently used as the final strengthening operation.

Author Contributions: O.M. carried out the literature analysis and paper writing; A.K. contributed to the discussion of results. All authors have read and agreed to the published version of the manuscript.

Funding: This research received no external funding.

Acknowledgments: Olexandra Marenych is thankful for a scholarship sponsored by the Defence Materials Technology Centre at the University of Wollongong (Australia), which was established under the initiative of the Australian Government's Defence Future Capability Technology Centre.

Conflicts of Interest: The authors declare no conflict of interest.

References

1. Waite, J.G.; Look, D.; Gayle, M. *Metals in America's Historic Buildings: Uses and Preservation Treatments*; US Department of the Interior, National Park Service, Cultural Resources: Washington, DC, USA, 1995.
2. Lippold, J.C.; DuPont, J.; Kiser, S.D. Alloying Additions, Phase Diagrams and Phase Stability. In *Welding Metallurgy and Weldability of Nickel-Base Alloys*; John Wiley & Sons: Hoboken, NJ, USA, 2009; Chapter 2; pp. 15–45.
3. Czajkowski, C.; Butters, M. *Investigation in Hardsurfacing a Nickel-Copper Alloy (Monel400)*; Report BNL-52651; Brookhaven National Laboratory: Upton, NY, USA, 2001.
4. Heckel, R.W.; Rickets, J.H.; Buchwald, J. Measurement of the degree of segregation in Monel 400 weld metal by X-ray line broadening. *Weld. J.* **1965**, *34*, 332–336.
5. Doherty, R.D.; Feest, E.A.; Holm, K. Dendritic solidification of Cu-Ni alloys: Part I. Initial growth of dendrite structure. *Metall. Mater. Trans. A* **1973**, *4*, 115–124. [CrossRef]
6. Dundar, S. Dendritic solidication in a copper nickel alloy. *Turkish J. Eng. Env. Sci.* **2004**, *28*, 129–134.
7. Algoso, P.; Hofmeister, W.; Bayuzick, R. Solidification velocity of undercooled Ni–Cu alloys. *Acta Mater.* **2003**, *51*, 4307–4318. [CrossRef]
8. Hou, H.; Li, Y.; Xu, X.; Zhao, Y.; Liu, F. Non-equilibrium effects on solid transition of solidification microstructure of deeply undercooled alloys. *Mater. Sci. Technol.* **2017**, *34*, 402–407. [CrossRef]
9. Arjmand, M.; Abbasi, S.; Taheri, A.K.; Momeni, A. Hot workability of cast and wrought Ni–42Cu alloy through hot tensile and compression tests. *Trans. Nonferrous Met. Soc. China* **2016**, *26*, 1589–1597. [CrossRef]
10. Ebrahimi, G.R.; Momeni, A.; Ezatpour, H.; Jahazi, M.; Bocher, P. Dynamic recrystallization in Monel400 Ni-Cu alloy: Mechanism and role of twinning. *Mater. Sci. Eng. A* **2019**, *744*, 376–385. [CrossRef]
11. Es-Said, O.; Zakharia, K.; Ventura, C.; Pfost, D.; Crawford, P.; Ward, T.; Raizk, D.; Foyos, J.; Marloth, R.; Zakharia, Z. Failure analysis of K-monel 500 (Ni–Cu–Al alloy) bolts. *Eng. Fail. Anal.* **2000**, *7*, 323–332. [CrossRef]
12. Harris, Z.D.; Burns, J.T. The effect of isothermal heat treatment on hydrogen environment-assisted cracking susceptibility in Monel K-500. *Mater. Sci. Eng. A* **2019**, *764*, 138249. [CrossRef]
13. Ramkumar, K.D.; Joshi, V.; Pandit, S.; Agrawal, M.; Kumar, O.S.; Periwal, S.; Manikandan, M.; Arivazhagan, N. Investigations on the microstructure and mechanical properties of multi-pass pulsed current gas tungsten arc weldments of Monel 400 and Hastelloy C276. *Mater. Des.* **2014**, *64*, 775–782. [CrossRef]

14. Mani, C.; Karthikeyan, R.; Kannan, S.; Periasamy, C. Optimization of tensile properties of 316L stainless steel and Monel 400 weld joints using genetic algorithm. *Mater. Today: Proc.* **2020**, *27*, 2846–2851. [CrossRef]
15. Heidarzadeh, A.; Chabok, A.; Pei, Y. Friction stir welding of Monel alloy at different heat input conditions: Microstructural mechanisms and tensile behavior. *Mater. Lett.* **2019**, *245*, 94–97. [CrossRef]
16. Available online: https://markets.businessinsider.com/commodities/nickel-price (accessed on 21 August 2020).
17. Available online: https://www.fastmarkets.com/commodities/exchange-data/lme-base-metal-prices-and-charts (accessed on 21 August 2020).
18. Available online: https://www.superiorsteel.in/blog/monel-alloy-400-k500-price-list (accessed on 21 August 2020).
19. Davis, J.R. Introduction to Nickel and Nickel Alloys. In *Nickel, Cobalt, and Their Alloys*; ASM Specialty Handbook; ASM International: Materials Park, OH, USA, 2000; Chapter 1.
20. High-Performance Alloys for Resistance to Aqueous Corrosion, Special Metals Corporation, Publication Number SMC-026. 2000. Available online: https://www.scribd.com/document/55871734/Nickel-Base (accessed on 27 August 2020).
21. Stoloff, N.S. Wrought and P/M superalloys. In *Properties and Selection: Irons, Steels, and High-Performance Alloys*; ASM Handbook; ASM International: Materials Park, OH, USA, 1990; Volume 1, pp. 950–980.
22. Lippold, J.C.; DuPont, J.; Kiser, S.D. Precipitation-Strengthened Nickel-Base Alloys. In *Welding Metallurgy and Weldability of Nickel-Base Alloys*; John Wiley & Sons: Hoboken, NJ, USA, 2009; Chapter 4; pp. 157–254.
23. Monel Alloy 400, High Performance Alloys. Available online: http://www.hpalloy.com (accessed on 27 August 2020).
24. *Health Hazard Evaluation Report: HETA-97-0141-2819*; Special Metals Corporation, Princeton Powder Division: Princeton, KY, USA, 2001.
25. Monel Alloy R-405, High Performance Alloys. Available online: http://www.hpalloy.com (accessed on 27 August 2020).
26. Dutta, R. Corrosion aspects of Ni–Cr–Fe based and Ni–Cu based steam generator tube materials. *J. Nucl. Mater.* **2009**, *393*, 343–349. [CrossRef]
27. Prabhu, A.G.; Sathishkumar, N.; Pravinkumar, K.; Kumar, P.M.; Balasubramanian, T.; Sudharsan, P. Heat treatment and analysis of nickel super alloy for gas turbine applications. *Mater. Today Proc.* **2020**. [CrossRef]
28. Ghosh, S.; Dey, G.; Dusane, R.; Grover, A. Improved pitting corrosion behaviour of electrodeposited nanocrystalline Ni–Cu alloys in 3.0wt.% NaCl solution. *J. Alloy. Compd.* **2006**, *426*, 235–243. [CrossRef]
29. Silaimani, S.M.; Vivekanandan, G.; Veeramani, P. Nano-nickel–copper alloy deposit for improved corrosion resistance in marine environment. *Int. J. Environ. Sci. Technol.* **2014**, *12*, 2299–2306. [CrossRef]
30. *Monel Alloy 401*; Publication SMC-084; Special Metals Corporation: New Hartford, NY, USA, 2004.
31. *Monel Alloy 404*; Publication SMC-059; Special Metals Corporation: New Hartford, NY, USA, 2004.
32. Nady, H.; Negem, M. Ni–Cu nano-crystalline alloys for efficient electrochemical hydrogen production in acid water. *RSC Adv.* **2016**, *6*, 51111–51119. [CrossRef]
33. Wang, G.; Li, W.; Huang, B.; Xiao, L.; Lu, J.; Zhuang, L. Exploring the composition—Activity relation of Ni–Cu binary alloy electrocatalysts for hydrogen oxidation reaction in alkaline media. *ACS Appl. Energy Mater.* **2019**, *2*, 3160–3165. [CrossRef]
34. Brooks, R.B. *Heat Treatment, Structure and Properties of Nonferrous Alloys*; ASM international: Materials Park, OH, USA, 1982.
35. Roth, H.A.; Davis, C.L.; Thomson, R. Modeling solid solution strengthening in nickel alloys. *Metall. Mater. Trans. A* **1997**, *28*, 1329–1335. [CrossRef]
36. Kako, K.; Kawakami, E.; Ohta, J.; Mayuzumi, M. Effects of various alloying elements on tensile properties of high purity Fe-18Cr-(14-16)Ni alloys at room temperature. *Mater. Trans.* **2002**, *43*, 155–162. [CrossRef]
37. Shang, S.L.; Kim, D.E.; Zacherl, C.L.; Wang, Y.; Du, Y.; Liu, Z.K. Effects of alloying elements and temperature on the elastic properties of dilute Ni-base superalloys from first-principles calculations. *J. Appl. Phys.* **2012**, *112*, 053515. [CrossRef]
38. Pathak, A.; Singh, A.K. Mechanical properties of Ni-based solid solution alloys: A first principles study. *J. Appl. Res. Technol.* **2017**, *15*, 449–453. [CrossRef]
39. Hargather, C.Z.; Shang, S.-L.; Liu, Z.-K. A comprehensive first-principles study of solute elements in dilute Ni alloys: Diffusion coefficients and their implications to tailor creep rate. *Acta Mater.* **2018**, *157*, 126–141. [CrossRef]

40. Yang, Z.-B.; Sun, J.; Lu, S.; Vitos, L. Assessing elastic property and solid-solution strengthening of binary Ni–Co, Ni–Cr, and ternary Ni–Co–Cr alloys from first-principles theory. *J. Mater. Res.* **2018**, *33*, 2763–2774. [CrossRef]
41. Al-Jarba, K.A.; Fuchs, G.E. Carbon-containing single-crystal nickel-based superalloys: Segregation behavior and carbide formation. *JOM* **2004**, *56*, 50–55. [CrossRef]
42. He, L.Z.; Zheng, Q.; Sun, X.F.; Hou, G.C.; Guan, H.R.; Hu, Z.Q. M23C6 precipitation behavior in a Ni-base superalloy M963. *J. Mater. Sci.* **2005**, *40*, 2959–2964. [CrossRef]
43. Dong, X.; Zhang, X.; Du, K.; Zhou, Y.; Jin, T.; Ye, H. Microstructure of carbides at grain boundaries in nickel-based superalloys. *J. Mater. Sci. Technol.* **2012**, *28*, 1031–1038. [CrossRef]
44. Kontis, P.; Kostka, A.; Raabe, D.; Gault, B. Influence of composition and precipitation evolution on damage at grain boundaries in a crept polycrystalline Ni-based superalloy. *Acta Mater.* **2019**, *166*, 158–167. [CrossRef]
45. Liu, T.; Yang, M.; Han, F.; Dong, J. Influence mechanism of silicon on carbide phase precipitation of a corrosion resistance nickel-based superalloy. *Materials* **2020**, *13*, 959. [CrossRef]
46. Kozar, R.; Suzuki, A.; Milligan, W.; Schirra, J.; Savage, M.; Pollock, T. Strengthening mechanisms in polycrystalline multimodal nickel-base superalloys. *Metall. Mater. Trans. A* **2009**, *40*, 1588–1603. [CrossRef]
47. Dai, P.; Zhang, C.; Wen, J.C.; Rao, H.C.; Wang, Q.T. Tensile Properties of Electrodeposited Nanocrystalline Ni-Cu Alloys. *J. Mater. Eng. Perform.* **2016**, *25*, 594–600. [CrossRef]
48. Ross, E.W.; Sims, C.T. Nickel-Base Alloys. In *Superalloys IIHigh Temperature Materials for Aerospace and Industrial Power*; Sims, C.T., Stoloff, N.S., Hagel, W.C., Eds.; Wiley: New York, NY, USA, 1987; pp. 97–133.
49. Dey, G.; Mukhopadhyay, P. Precipitation in the NiCu-base alloy monel K-500. *Mater. Sci. Eng.* **1986**, *84*, 177–189. [CrossRef]
50. Barbosa, C.; Nascimento, J.; Caminha, I.; Abud, I. Microstructural aspects of the failure analysis of nickel base superalloys components. *Eng. Fail. Anal.* **2005**, *12*, 348–361. [CrossRef]
51. Krishna Reddy, L. *Principles of Engineering Metallurgy*; New Age International: New Delhi, India, 2007.
52. *Monel Alloy R-405*; Publication SMC-085; Special Metals Corporation: New Hartford, NY, USA, 2004.
53. *Monel Alloy K-500*; Publication SMC-062; Special Metals Corporation: New Hartford, NY, USA, 2004.
54. Hurlbatt, J.D. Hot rolling of sheet: Nickel-based alloys. *Met. Technol.* **1975**, *2*, 326–330. [CrossRef]
55. Guinier, A.; Lorrain, P.; Lorrain, D.S.M.; Gillis, J. X-Ray diffraction in crystals, imperfect crystals, and amorphous bodies. *Phys. Today* **1964**, *17*, 70. [CrossRef]
56. Product Handbook of High Performance Ni Alloys, Special Metals Corporation. Available online: www.specialmetals.com (accessed on 27 August 2020). Special Metals Corporation.
57. Fabrication of Nickel Alloys, Bulletin, Special Metals Corporation. Available online: www.specialmetals.com (accessed on 27 August 2020).
58. Ai, J.-H.; Ha, H.M.; Gangloff, R.P.; Scully, J.R. Hydrogen diffusion and trapping in a precipitation-hardened nickel–copper–aluminum alloy Monel K-500 (UNS N05500). *Acta Mater.* **2013**, *61*, 3186–3199. [CrossRef]
59. George, E.P.; Liu, C.T. Alloy Design of Ordered Intermetallics. In *MRS Proceedings*; Cambridge University Press (CUP): Cambridge, UK, 1990; Volume 186, pp. 913–942.
60. Lifshitz, I.; Slyozov, V. The kinetics of precipitation from supersaturated solid solutions. *J. Phys. Chem. Solids* **1961**, *19*, 35–50. [CrossRef]
61. Liu, C.; Li, Y.; Zhu, L.; Shi, S. Effect of coherent lattice mismatch on the morphology and kinetics of ordered precipitates. *J. Mater. Eng. Perform.* **2018**, *27*, 4968–4977. [CrossRef]
62. Baker, H. (Ed.) *Alloy. Phase Diagrams*; ASM International: Materials Park, OH, USA, 1992.
63. Sims, C.T. Cobalt-base alloys. In *The Superalloys*; Sims, C.T., Hagel, W.C., Eds.; John Wiley & Sons: New York, NY, USA, 1972; pp. 145–174.
64. Ardell, A.J.; Nicholson, R.B.; Eshelby, J.D. On the modulated structure of aged Ni-Al alloys (with an appendix on the elastic interaction between inclusions). *Acta Metall.* **1966**, *14*, 1295–1309. [CrossRef]
65. Ben Israel, D.; Fine, M. Precipitation studies in Ni-10 at.% Ti. *Acta Metall.* **1963**, *11*, 1051–1059. [CrossRef]
66. Decker, R.F.; Sims, C.T. The metallurgy of Nickel-base alloys. In *The Superalloys*; Sims, C.T., Hagel, W.C., Eds.; John Wiley & Sons: New York, NY, USA, 1972; pp. 33–77.
67. Hansen, M.; Anderko, K.; Salzberg, H.W. Constitution of binary alloys. *J. Electrochem. Soc.* **1958**, *105*, 260C. [CrossRef]
68. Thornton, P.H.; Davies, P.H.; Johnston, T.L. Temperature dependence of the flow stress of the gamma prime phase based upon Ni3Al. *Metall. Trans. A* **1970**, *1*, 207–218.

69. Dey, G.K.; Tewari, R.; Rao, P.; Wadekar, S.L.; Mukhopadhyay, P. Precipitation hardening in nickel-copper base alloy Monel K-500. *Metall. Mater. Trans. A* **1993**, *24*, 2709–2719. [CrossRef]
70. Dupont, J.N.; Notis, M.R.; Marder, A.R.; Robino, C.V.; Michael, J.R. Solidification of Nb-bearing superalloys: Part I. Reaction sequences. *Metall. Mater. Trans. A* **1998**, *29*, 2785–2796. [CrossRef]
71. Davis, J.R. Fabrication and Finishing of Nickel Alloys, Heat Treating of Nickel Alloys. In *Nickel, Cobalt, and Their Alloys*; ASM Specialty Handbook; ASM International: Materials Park, OH, USA, 2000; Chapter 3.
72. Murr, L.E.; Smith, P.J.; Gilmore, C.M. Relative interfacial free energies in pure nickel, dispersion hardened nickel, and a precipitation hardened nickel-base alloy. *Philos. Mag.* **1968**, *17*, 89–106. [CrossRef]
73. Kukliński, M.; Bartkowska, A.; Przestacki, D. Microstructure and selected properties of Monel 400 alloy after laser heat treatment and laser boriding using diode laser. *Int. J. Adv. Manuf. Technol.* **2018**, *98*, 3005–3017. [CrossRef]
74. Krelling, A.P.; Melo, F.S.; Almeida, E.A.D.S.D.; Da Costa, C.E.; Milan, J.C.G. Microstructure and properties of borided Monel 400 alloy. *Mater. Res. Express* **2019**, *6*, 106410. [CrossRef]
75. Gallagher, P.C.J. The influence of alloying, temperature, and related effects on the stacking fault energy. *Metall. Trans.* **1970**, *1*, 2429–2461.
76. Kotval, P.S. Identification of the strengthening phase in "Inconel" alloy 718. *Trans. AIME* **1968**, *242*, 1764–1765.
77. Dillamore, I.L. The stacking fault energy dependence of the mechanisms of deformation in fcc metals. *Metall. Trans.* **1970**, *1*, 2463–2470.
78. Deléhouzée, L.; Deruyttere, A. The stacking fault density in solid solutions based on copper, silver, nickel, aluminium and lead. *Acta Metall.* **1967**, *15*, 727–734. [CrossRef]
79. Haouala, S.; Segurado, J.; Llorca, J. An analysis of the influence of grain size on the strength of FCC polycrystals by means of computational homogenization. *Acta Mater.* **2018**, *148*, 72–85. [CrossRef]
80. Ishikawa, K.; Tanimura, S. Strain rate sensitivity of flow stress at low temperatures in 304n stainless steel. *Int. J. Plast.* **1992**, *8*, 947–958. [CrossRef]
81. Gray, G.T.; Chen, S.R.; Vecchio, K.S. Influence of grain size on the constitutive response and substructure evolution of MONEL 400. *Metall. Mater. Trans. A* **1999**, *30*, 1235–1247. [CrossRef]
82. Parker, E.; Hazlett, T. *Principles of Solution Hardening*; Technical report No. 12; University of California: Berkley, CA, USA, 1953.
83. Decker, R.F.; Mihalisin, J.R. Coherency strains in gamma prime hardened nickel alloys. *Trans. ASM Q.* **1969**, *62*, 481–489.
84. Mishima, Y.; Ochiai, S.; Hamao, N.; Yodogawa, M.; Suzuki, T. Solid Solution Hardening of Nickel—Role of Transition Metal and B-subgroup Solutes—. *Trans. Jpn. Inst. Met.* **1986**, *27*, 656–664. [CrossRef]
85. Pyczak, F.; Devirent, B.; Mughrabi, H. The effects of different alloying elements on the thermal expansion coefficients, lattice constants and misfit of nickel-based superalloys Investigated by X-Ray Diffraction. *Superalloys 718 Metallurgy Appl. (1989)* **2004**, 827–836. [CrossRef]
86. Huther, W.; Reppich, B. Interaction of dislocations with coherent, stress-free, ordered particles. *Zeitschrift für Metallkunde* **1978**, *69*, 628–634.
87. Lippold, J.C.; DuPont, J.; Kiser, S.D. Solid-solution Strengthened Ni-base Alloys. In *Welding Metallurgy and Weldability of Nickel-Base Alloys*; John Wiley & Sons: Hoboken, NJ, USA, 2009; Chapter 3; pp. 47–156.
88. Wang, Z.X.; Liu, S.; Yuan, S.; Yang, C. Strength and ductility of Ni-Cu-Base alloy Monel K-500. *Trans. NFSoc China* **1995**, *5*, 111–115.
89. Biss, V.; Sponseller, D.L. Effect of molybdenum on gamma prime coarsening and on elevated-temperature hardness in some experimental Ni-base superalloys. *Metall. Trans. A* **1973**, *4*, 1953–1960. [CrossRef]
90. Guard, R.W.; Westbrook, J.H. Alloying behaviour of Ni3Al (γ phase). *Trans. AIME* **1959**, *215*, 807–813.
91. Gallai, Y.S.; Karmanova, E.G.; Zorina, N.A.; Grigor'Eva, M.M. Cold working and recrystallization of nickel alloys. *Met. Sci. Heat Treat.* **1967**, *9*, 323–324. [CrossRef]
92. Marenych, O.; Kostryzhev, A.G.; Pan, Z.; Li, H.; Van Duin, S. Comparative effect of Mn/Ti solute atoms and TiC/Ni3(Al,Ti) nano-particles on work hardening behaviour in Ni Cu alloys fabricated by wire arc additive manufacturing. *Mater. Sci. Eng. A* **2019**, *753*, 262–275. [CrossRef]
93. Martens, V.; Nembach, E. Strengthening of the nimonic alloy PE 16 by ordered particles of Ni3(Al, Ti). *Acta Metall.* **1975**, *23*, 149–153. [CrossRef]
94. Smith, G.D.; Baker, B.A. Nickel and Its Alloys. In *Mechanical Engineers' Handbook*; Wiley & Sons: Hoboken, NJ, USA, 2015; pp. 1–22.

95. Watson, J.F.; Christian, J.L. Low-Temperature Properties of K-monel, inconel-X, Rene´ 41, Haynes 25, and Hastelloy B Sheet alloys. *J. Basic Eng.* **1962**, *84*, 265–277. [CrossRef]
96. Hurlich, A. Low Temperature Materials. In *Chemical Engineering*; McGraw-Hill Publishing Go. Inc.: New York, NY, USA, 1963; pp. 311–325.
97. Ramkumar, K.D.; Arivazhagan, N.; Narayanan, S.; Mishra, D. Hot corrosion behavior of monel 400 and AISI 304 dissimilar weldments exposed in the molten salt environment containing Na2SO4 + 60% V2O5 at 600 °C. *Mater. Res.* **2014**, *17*, 1273–1284. [CrossRef]
98. Raffeis, I.; Adjei-Kyeremeh, F.; Vroomen, U.; Westhoff, E.; Bremen, S.; Hohoi, A.; Bührig-Polaczek, A. Qualification of a Ni–Cu Alloy for the Laser Powder Bed Fusion Process (LPBF): Its Microstructure and Mechanical Properties. *Appl. Sci.* **2020**, *10*, 3401. [CrossRef]
99. Marenych, O.; Ding, D.; Pan, Z.; Kostryzhev, A.G.; Li, H.; Van Duin, S. Effect of chemical composition on microstructure, strength and wear resistance of wire deposited Ni-Cu alloys. *Addit. Manuf.* **2018**, *24*, 30–36. [CrossRef]